Lead nitrate hydroxide: A strong second-order optical nonlinearity acentric crystal with high laser damage thresholds

A. H. Reshak

Lead nitrate hydroxide: A strong second-order optical nonlinearity acentric crystal with high laser damage thresholds

A. H. Reshak[a)]

New Technologies-Research Centre, University of West Bohemia, Univerzitni 8, 306 14 Pilsen,
Czech Republic and Center of Excellence Geopolymer and Green Technology, School of Material
Engineering, University Malaysia Perlis, 01007 Kangar, Perlis, Malaysia

A comprehensive theoretical calculation for the complex first-order linear and the second-order non-linear optical dispersion of acentric lead nitrate hydroxide ($Pb_{16}(OH)_{16}(NO_3)_{16}$) single crystals was performed based on the experimental crystallographic data obtained by Chang *et al*. [Inorg. Chem. **53**, 3320–3325 (2014)]. Calculations show an energy band gap of about 3.70 eV, in close agreement to the measured one (3.78 eV). The energy gap value confirms that the $Pb_{16}(OH)_{16}(NO_3)_{16}$ single crystal exhibits an exceptional laser damage threshold. The complex first-order linear optical dispersion helps to get deep insight into the electronic structure and reveals the existence of considerable anisotropy, negative uniaxial anisotropy, and positive birefringence. The calculated second harmonic generation of $Pb_{16}(OH)_{16}(NO_3)_{16}$ at wavelength ($\lambda = 1064$ nm) shows a good agreement with the reported measured value. In addition, the microscopic first hyperpolarizability was obtained at the static limit and at the wavelength 1064 nm. © *2016 AIP Publishing LLC*. [http://dx.doi.org/10.1063/1.4943650]

I. INTRODUCTION

The promising applications of nonlinear optical materials (NLO) for second harmonic generation (SHG), sum or difference frequency mixing, optical parametric oscillation (OPO) or amplification (OPA), and as efficient photonic devices[1–7] have resulted in the development of different varieties of novel inorganic and organic NLO crystals.[8] The SHG is a NLO phenomenon which is related to the nonlinear electrical susceptibility. Developing highly efficient NLO crystals for ultra-violet (UV) and deep-UV applications is important for laser spectroscopy and laser processing, including laser-tailoring of molecules and optical triggering. It has been reported that borate crystals are extremely useful for solid state UV lasers.[9–11] The NLO properties of the oxo-borate materials have been reported and found to be comparable to those of β-BaB$_2$O$_4$ (BBO) for the SHG.[8] The investigation of the structural characteristics of borate crystals helps to understand the importance of borate crystals in the field of NLO. The boron atom has two types of hybridized orbitals, the planar sp^2 and the three dimensional sp^3, to coordinate three or four oxygen atoms forming BO_3^{3-}, BO_3^{4-}, or BO_4^{5-} clusters. Further, these clusters comprise several different typical BxOy groups, and therefore, various types of borate crystals can be constructed based on these infrastructures, for example, the isolated BO$_3$ group in NAB and CReOB, the B$_3$O$_6$ group in BBO, the B$_3$O$_7$ group in LBO, and the B$_5$O$_{10}$ group in KB$_5$. This is a very attractive phenomenon discovered in inorganic borate crystals. Therefore, it is very interesting to study the influence of BO_3^{3-}, BO_3^{4-}, or BO_4^{5-} clusters on the second-order NLO response of various types of borate crystals, so as to get some useful information in searching for new NLO

materials.[8] Bian *et al*.[12] have used the first principle method to calculate the birefringence values of five lead borates, $Pb_8B_9O_{21}F$, $PbBiBO_4$, Pb_3BO_4F, $Pb_6B_3O_{10}Cl$, and Pb_2BO_3F with network B–O structure or isolated BO$_3$ groups. The calculations show that $PbBiBO_4$, Pb_3BO_4F, and Pb_2BO_3F have a large birefringence, greater than 0.1. Pb_2BO_3F, especially, is the first compound with large birefringence above 0.08 among positive uniaxial borate crystals. It has been found that the parallel arrangement of fundamental building units is not the only light anisotropy active characteristics. In the further research of Pb_2BO_3F, polarization disproportionation via a visualized model is first put forward for identifying the origin of large birefringence, which will be helpful to search for new optical materials with suitable birefringence. Li *et al*.[13] have investigated the electronic structures and optical properties of a class of lead borates, $Pb_2B_5O_9Cl$, $BaPb[B_5O_9(OH)]\cdot H_2O$, and $Ba_2Pb(B_3O_6)_2$, to uncover the influence of the lead atom on the band gap and SHG response. It has been found that $BaPb[B_5O_9(OH)]\cdot H_2O$ and $Ba_2Pb(B_3O_6)_2$ have little band gap redshift due to their weak distortion and stereochemical activity. The intensity of the lead lone-pair stereochemical activity plays an important role in determining the reduction of the band gap. However, it is still desirable to find materials with promising NLO properties. Therefore, similar to BO_3^{3-}, BO_3^{4-}, or BO_4^{5-} clusters, the NO_3^- clusters can be the sources of strong microscopic second order susceptibilities in the UV and deep UV regions. Several research groups have investigated the NLO properties of NO_3^- containing materials.[14] Recently, Chang *et al*.[15] have reported the synthesis of the first example of the lead nitrate hydroxide NLO crystal $Pb_{16}(OH)_{16}(NO_3)_{16}$ with a large SHG response of about 3.5 times that of the well-known NLO crystal KH_2PO_4 (KDP). It has been found that lead nitrate hydroxide ($Pb_{16}(OH)_{16}(NO_3)_{16}$) is a type I phase-matchable crystal and the local dipole moment of PbO_n

---

a)Author to whom correspondence should be addressed. Electronic mail: maalidph@yahoo.co.uk

polyhedra is larger than that of NO_3^- triangles. Therefore, based on the investigation of Chang et al. and due to the lack of information about the complex first-order linear and second-order non-linear optical dispersion, we have performed comprehensive density functional calculations to investigate the electronic structure and hence the complex first-order linear optical dispersion, birefringence, complex second-order non-linear optical dispersion, and microscopic first hyperpolarizability. Calculations were performed using the all-electron-full-potential method within two exchange and correlation (XC) potentials so as to ascertain the influence of the XC potentials on the electronic band structure, energy band gap, and hence the resulting linear and nonlinear optical properties.

II. METHODOLOGY

Based on the density functional theory (DFT) within the all-electron full-potential linearized augmented plane wave plus local orbitals (FP-LAPW+lo) method, as implemented in the WIEN2k package,[16] comprehensive theoretical calculations were performed to calculate the electronic properties of $Pb_{16}(OH)_{16}(NO_3)_{16}$. The crystallographic data reported by Chang et al.[15] were used as input to perform the geometrical relaxation. The experimental lattice parameters[15] were optimized as shown in Table S1 of the supplementary material.[19] The experimental atomic positions[15] were relaxed by minimizing the forces acting on each atom; we assume that the structure is totally relaxed when the forces on each atom reach values less than 1 mRy/a.u. The relaxed atomic positions in comparison with the experimental data[15] are listed in Table S2 of the supplementary material.[19] The geometrical relaxation was achieved by using Perdew-Burke-Ernzerhof generalized gradient approximation (PBE-GGA).[17] From the relaxed geometry, the electronic band structure was obtained using PBE-GGA and the recently modified Becke-Johnson potential (mBJ).[18] After detailed comparison between the two exchange-correlation potentials (see Figs. S3–S5 of the supplementary material[19]), we found that mBJ succeeds by a large amount in bringing the calculated energy gap closer to the experimental one. Therefore, the results obtained by mBJ are shown below. Based on the calculated band structure, the complex first-order linear and second-order non-linear optical dispersion are obtained. The $Pb_{16}(OH)_{16}(NO_3)_{16}$ crystallizes in the monoclinic space group with four formulas per unit cell.[15] The unit cell consists of 112 atoms, 16 Pb atoms, 16 nitrates, 16 hydrogen, and 64 oxygen atoms. Each N atom connects to three oxygen atoms to form the $[NO_3]^-$ triangle; the other oxygen atoms connect to Pb atoms to form the PbO_n polyhedra. The unit cell is illustrated in Fig. S1 of the supplementary material.[19] To insure that no charge leakage is left out of the atomic sphere cores, the minimum radius of the muffin-tin spheres (R_{MT}) values are set as 2.24 a.u. for Pb atoms, 1.03 a.u. for N atoms, 1.08 a.u. for O atoms, and 0.59 for H atoms. The R_{MT}'s were chosen in such a way that the spheres did not overlap. The basis functions inside the interstitial region were expanded up to $R_{MT} \times K_{max} = 7.0$ and inside the atomic spheres for the wave function, in order to achieve the total energy convergence. The potential for the construction of basis functions inside the sphere of the muffin tin was spherically symmetric, whereas outside the sphere it was constant.[20] The maximum value of l was taken as $l_{max} = 10$, while the charge density is Fourier expanded up to $G_{max} = 12.0(a.u)^{-1}$. A self-consistency is obtained by using 300 $\bar{k}$ points in the irreducible Brillouin zone (IBZ). Since the total energy of the system is stable within 0.00001 Ry, the self-consistent calculations are converged. The electronic band structure calculation was performed within 1000 $\bar{k}$ points in the *IBZ*. While the linear and nonlinear optical susceptibilities were obtained by using 2000 $\bar{k}$ points in the *IBZ*. The first-principle calculations were proved to be a powerful and useful tool to predict the crystal structure and physical properties before synthesizing of a new material.[21–23]

III. RESULTS AND DISCUSSION

A. Complex first-order linear optical dispersion

To gain further insight into the electronic structure, the complex first-order linear optical dielectric functions are calculated on the basis of the DFT. The electronic structure shows that the B−O anionic groups are the main factor to influence the band gap and hence the linear optical properties.[12] The calculations of the optical dielectric functions involve the energy eigenvalues and electron wave functions. These are the natural outputs of band structure calculations. Therefore, based on the calculated band structure, we have performed calculations for the imaginary part of the interband frequency-dependent dielectric function using the expressions taken from Refs. 24 and 25

$$\varepsilon_2^{ij}(\omega) = \frac{8\pi^2\hbar^2e^2}{m^2V}\sum_k\sum_{cv}(f_c - f_v)$$
$$\times \frac{p_{cv}^i(k)p_{vc}^j(k)}{E_{vc}^2}\delta[E_c(k) - E_v(k) - \hbar\omega], \quad (1)$$

where m, e, and $\hbar$ are the electron mass, charge, and Planck's constant, respectively. f_c and f_v represent the Fermi distributions of the conduction and valence bands, respectively. The term $p_{cv}^i(k)$ denotes the momentum matrix element transition from the energy level c of the conduction band to the level v of the valence band at certain **k**-point in the BZ and V is the unit cell volume. The linear optical properties are calculated using the optical code implemented in the WIEN2k package,[16] for more details please see the user guide, Refs. 26 and 25.

It is clear that the band gap value comes in the denominator of the above expression which causes the result to be very sensitive to the energy band gap value. It is well-known that the DFT leads to an underestimated energy gap value. In the DFT, by solving the Kohn-Sham equations, we map an interacting many-body system to a non-interacting hypothetical system which has the same electron density. The price that we pay is the definition of a new functional that is called the exchange-correlation functional. Unfortunately, the exact form of the XC functional is unknown. Thus, the accuracy of the results will be sensitive to the selection of the XC functional which can play a major role. Therefore, based on our

experience in using different XC functionals (LDA, PBE-GGA, EV-GGA, LDA-mBJ, and PBE-GGA-mBJ) on several systems whose energy band gaps are known experimentally,[27–29] in those previous calculations we found that the PBE-GGA-mBJ gives a very good agreement with experimental data.[27–29] This motivated us to use PBE-GGA-mBJ to calculate the band structure and hence the first-order linear optical dielectric functions of $Pb_{16}(OH)_{16}(NO_3)_{16}$. The mBJ is a modified Becke-Johnson potential, which allows the calculation of the energy band gap with the accuracy similar to

that of the very expensive GW calculations.[18] It is a local approximation to an atomic "exact-exchange" potential and a screening term. It has been found that $Pb_{16}(OH)_{16}(NO_3)_{16}$ has a direct band gap of about 3.13 eV (PBE-GGA) and 3.70 eV (mBJ). The latter shows a close agreement with the measured one (3.78 eV).[15] Therefore, a material with such an energy band gap value is expected to possess a high laser damage threshold.[30,31] Since the investigated compound has monoclinic symmetry, there are several components of the dielectric tensor. We will concentrate only on the major
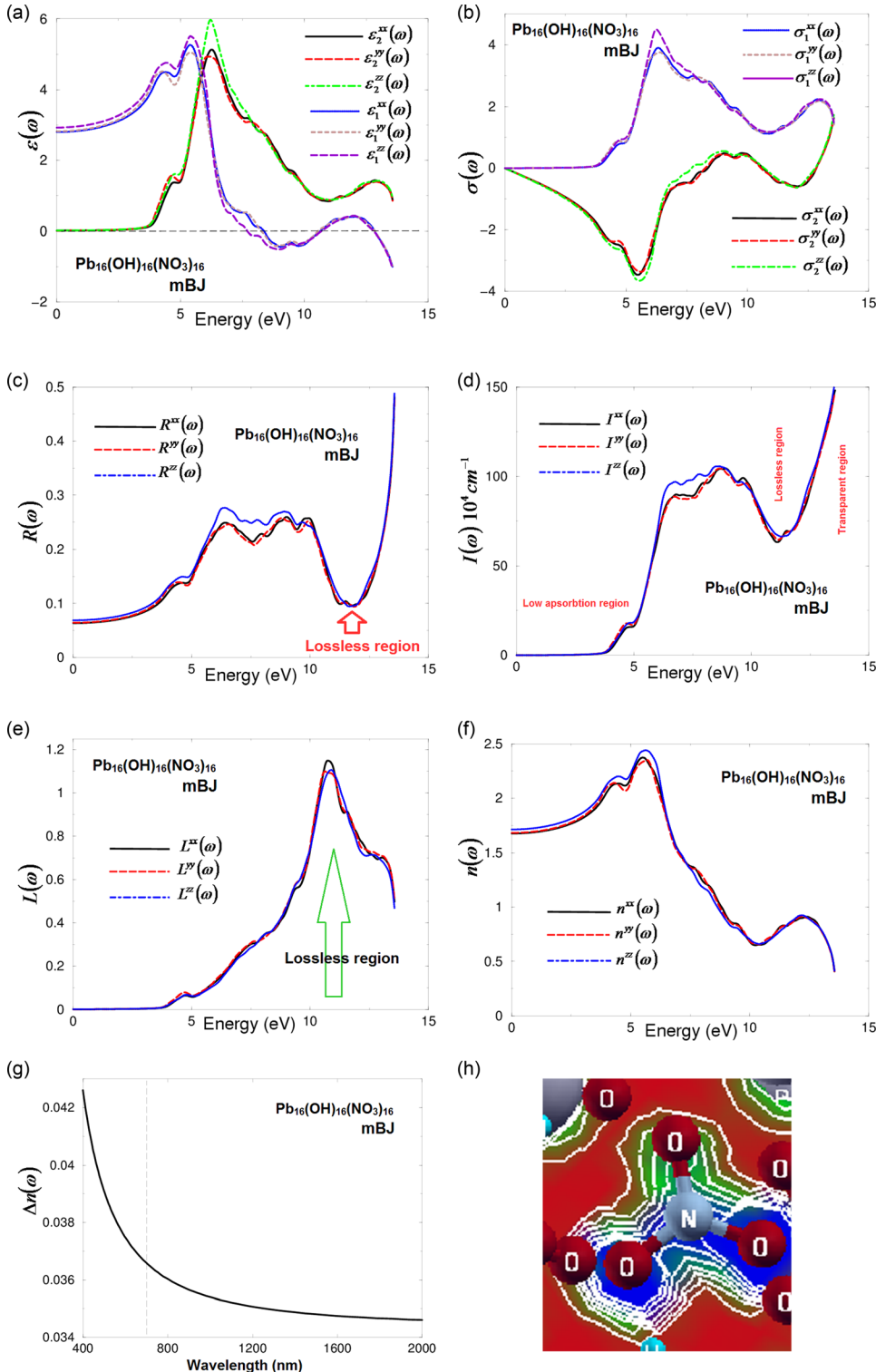

FIG. 1. (a) Calculated $\varepsilon_2^{xx}(\omega)$ (dark solid curve-black), $\varepsilon_2^{yy}(\omega)$ (light long dashed curve-red), and $\varepsilon_2^{zz}(\omega)$ (light dotted dashed curve-green) along with Calculated $\varepsilon_1^{xx}(\omega)$ (dark solid curve-blue), $\varepsilon_1^{yy}(\omega)$ (light dashed curve-brown), and $\varepsilon_1^{zz}(\omega)$ (light sold curve-violet); (b) calculated $\sigma_2^{xx}(\omega)$ (dark solid curve-black), $\sigma_2^{yy}(\omega)$ (light dashed curve-red), and $\sigma_2^{zz}(\omega)$ (light dotted dashed curve-green) along with calculated $\sigma_1^{xx}(\omega)$ (dark solid curve-blue), $\sigma_1^{yy}(\omega)$ (light dashed curve-red brown), and $\sigma_1^{zz}(\omega)$ (light solid curve-violet); (c) calculated $R^{xx}(\omega)$ (dark solid curve-black), $R^{yy}(\omega)$ (light dashed curve-red), and $R^{zz}(\omega)$ (light dotted dashed curve-blue); (d) calculated absorption coefficient $I^{xx}(\omega)$ (dark solid curve-back), $I^{yy}(\omega)$ (light dashed curve-red), and $I^{zz}(\omega)$ (light dotted dashed curve-blue) spectrum for $LiMoO_3(IO_3)$, the absorption coefficient in $10^4 cm^{-1}$; (e) calculated loss function $L^{xx}(\omega)$ (dark solid curve-back), $L^{yy}(\omega)$ (light dashed curve-red), and $L^{zz}(\omega)$ (light dotted dashed curve-blue) spectrum; (f) calculated refractive indices $n^{xx}(\omega)$ (dark solid curve-black), $n^{yy}(\omega)$ (light dashed curve-red), and $n^{zz}(\omega)$ (light dotted dashed curve-blue) spectrum; (g) calculated birefringence $\Delta n(\omega)$; and (h) the electron cloud of the NO_3 anionic groups which exhibit planar shape with conjugated electron orbitals which make the NO_3 anionic groups are the main source of the large birefringence in $Pb_{16}(OH)_{16}(NO_3)_{16}$.

components, corresponding to an electric field perpendicular and parallel to the c-axis. These are $\varepsilon^{xx}(\omega)$, $\varepsilon^{yy}(\omega)$, and $\varepsilon^{zz}(\omega)$, which completely characterize the linear optical properties of the monoclinic system. The calculated imaginary part $\varepsilon_2^{xx}(\omega)$, $\varepsilon_2^{yy}(\omega)$, and $\varepsilon_2^{zz}(\omega)$ of the major components of the first-order linear optical dielectric functions for $Pb_{16}(OH)_{16}(NO_3)_{16}$ along the polarization directions [100], [010], and [001] are illustrated in Fig. 1(a). It has been found that absorption edges of $\varepsilon_2^{xx}(\omega)$, $\varepsilon_2^{yy}(\omega)$, and $\varepsilon_2^{zz}(\omega)$ are located at 3.70 eV, in a good agreement with the measured ones (see Fig. S2 of the supplementary material[19]). The edges of optical absorption give the threshold for direct optical transitions between the VBM (Pb-6s/6p/5d,4f, O-2p) and the CBM (N-2s/2p, Pb-6p/5d/4f). Beyond the absorption edges, a rapid increase occurs in the optical spectra to form the fundamental peaks of $\varepsilon_2^{xx}(\omega)$, $\varepsilon_2^{yy}(\omega)$, and $\varepsilon_2^{zz}(\omega)$ at around 6.25 eV. These are due to the optical transition from O-2s/2p, Pb-6s/6p/5d/4f, H-1s at the VBs to N-2s/2p, O-2s/2p, Pb-6s/6p/5d/4f bands at the CBs, according to the selection rules which present the maximum absorption (see Fig. 1(a) and Fig. S3 of the supplementary material[19]). After that, a prompt reduction occurs in the spectral structure to form the tail of the spectra. In order to identify the observed spectral structures, we need to look at the magnitude of the optical matrix elements. The observed spectral structures would correspond to those transitions that have large optical matrix elements. We have used our calculated electronic band structure and the angular momentum resolved projected density of states to map the allowed optical transitions following the selection rules. For simplicity, we have labeled the optical transitions as A, B, and C. The A transitions are responsible for the optical spectral structures between 0.0 and 5.0 eV, the B transitions represent 5.0–10.0 eV, and the C transitions represent the spectral structures between 10.0 and 14.0 eV (see Fig. S3 of the supplementary material[19]).

The real part of the first-order linear optical dielectric functions along the polarization directions [100], [010], and [001] are obtained by means of the Kramers-Kronig transformation,[24,25] as shown in Fig. 1(a). The vanishing frequency value in the dielectric function defines the static electronic dielectric constant by $\varepsilon_\infty = \varepsilon_1(0)$. These values are listed in Table I. Furthermore, the calculated real part of the optical dielectric functions can give information about the energy gaps, since the calculated static electronic dielectric constant $\varepsilon_\infty = \varepsilon_1(0)$ is inversely related to the energy gap; this can be explained on the basis of the Penn model.[32] One of the important features of the optical spectra is the plasmon oscillations ω_p^{xx}, ω_p^{yy}, and ω_p^{zz}. The plasmon oscillations are associated with inter-band transitions that occur at energies where optical spectra of $\varepsilon_1^{xx}(\omega)$, $\varepsilon_1^{yy}(\omega)$, and $\varepsilon_1^{zz}(\omega)$ cross zero. The values of ω_p^{xx}, ω_p^{yy}, and ω_p^{zz} are presented in Table I. The other important feature is the uniaxial anisotropy ($\delta\varepsilon$), which can be calculated from $\varepsilon_1^{xx}(0)$, $\varepsilon_1^{yy}(0)$, $\varepsilon_1^{zz}(0)$, and $\varepsilon_1^{average}(0)$. It has been found that $Pb_{16}(OH)_{16}(NO_3)_{16}$ exhibits negative $\delta\varepsilon$, as shown in Table I. The $[NO_3]^-$ groups are the main contributors to the optical anisotropy; in addition, Pb^{2+} cations may also contribute to the optical anisotropy due to the repulsion interactions of the lone pairs of Pb^{2+} cations.[12] Furthermore, the high electron density configuration and strong anisotropy of N-O

TABLE I. The calculated energy band gap in comparison with the experimental value, $\varepsilon_1^{xx}(0)$, $\varepsilon_1^{yy}(0)$, $\varepsilon_1^{zz}(0)$, $\varepsilon_1^{average}(0)$, $\delta\varepsilon$, ω_p^{xx}, ω_p^{yy}, ω_p^{zz}, $n^{xx}(0)$, $n^{yy}(0)$, $n^{zz}(0)$, $\Delta n(0)$, $\Delta n(\omega)$ at $\lambda = 400$ nm and $\Delta n(\omega)$ at $\lambda = 700$ nm.

	$Pb_{16}(OH)_{16}(NO_3)_{16}$	
	This work	Exp.
Eg (eV)	3.7	3.78[a]
$\varepsilon_1^{xx}(0)$	2.805	
$\varepsilon_1^{yy}(0)$	2.805	
$\varepsilon_1^{zz}(0)$	2.931	
$\varepsilon_1^{average}(0)$	2.847	
$\delta\varepsilon$	− 0.044	
ω_p^{xx}	8.394	
ω_p^{yy}	8.285	
ω_p^{zz}	7.714	
$n^{xx}(0)$	1.674	
$n^{yy}(0)$	1.674	
$n^{zz}(0)$	1.712	
$\Delta n(0)$	0.038	
$\Delta n(\omega)$ at $\lambda = 400$ nm	0.0423	
$\Delta n(\omega)$ at $\lambda = 700$ nm	0.0365	

[a]Reference 15 (experimental work).

groups indicate the main contribution of NO$_3$ groups to the optical anisotropy. The frequency-dependent optical conductivity (Fig. 1(b)) can be obtained from the complex first-order linear optical dielectric function following the expression $\varepsilon(\omega) = \varepsilon_1(\omega) + i\varepsilon_2(\omega) = 1 + \frac{4\pi i\sigma(\omega)}{\omega}$.[24,25] It consists of the imaginary and real parts; therefore, it completely characterizes the linear optical properties. The imaginary part $\sigma_2^{xx}(\omega)$, $\sigma_2^{yy}(\omega)$, and $\sigma_2^{zz}(\omega)$ between 0.0 and the values of ω_p^{xx}, ω_p^{yy}, and ω_p^{zz} exhibit overturned features of $\varepsilon_2^{xx}(\omega)$, $\varepsilon_2^{yy}(\omega)$, and $\varepsilon_2^{zz}(\omega)$, whereas the real parts $\sigma_1^{xx}(\omega)$, $\sigma_1^{yy}(\omega)$, and $\sigma_1^{zz}(\omega)$ show similar features to those of $\varepsilon_2^{xx}(\omega)$, $\varepsilon_2^{yy}(\omega)$, and $\varepsilon_2^{zz}(\omega)$.

The optical reflectivity spectra of $Pb_{16}(OH)_{16}(NO_3)_{16}$ along the polarization directions [100], [101], and [001] are shown in Fig. 1(c). It has been found that at low energies the compound exhibits low reflectivity. The first reflectivity maxima occur at around 6.5 eV, followed by the first reflectivity minima which are situated at around 7.5 eV, confirming the occurrence of a collective plasmon resonance in concordance with our observation in Fig. 1(a). At higher energies, the region confined between 11.0 and 12.0 eV represents the lossless region.

Fig. 1(d) illustrates the absorption coefficient of $Pb_{16}(OH)_{16}(NO_3)_{16}$; it can be divided into four regions: the low absorption region, high absorption region, lossless region, and high transparent region. The absorption edges of the three tensor components along the polarization directions [100], [101], and [001] occur at 3.7 eV, in concordance with the measured ones (3.78 eV)[15] (see Fig. S2 of the supplementary material[19]). Fig. 1(e) represents the loss function's peaks, which are initiated at the values of the plasma frequencies ω_p^{xx}, ω_p^{yy}, and ω_p^{zz}. These peaks represent the negative part of $\varepsilon_1^{xx}(\omega)$, $\varepsilon_1^{yy}(\omega)$, and $\varepsilon_1^{zz}(\omega)$.

The calculated linear optical properties show a considerable anisotropy, which favors an important quantity in the SHG and OPO due to better fulfilling of phase-matching conditions determined by birefringence. Birefringence is important
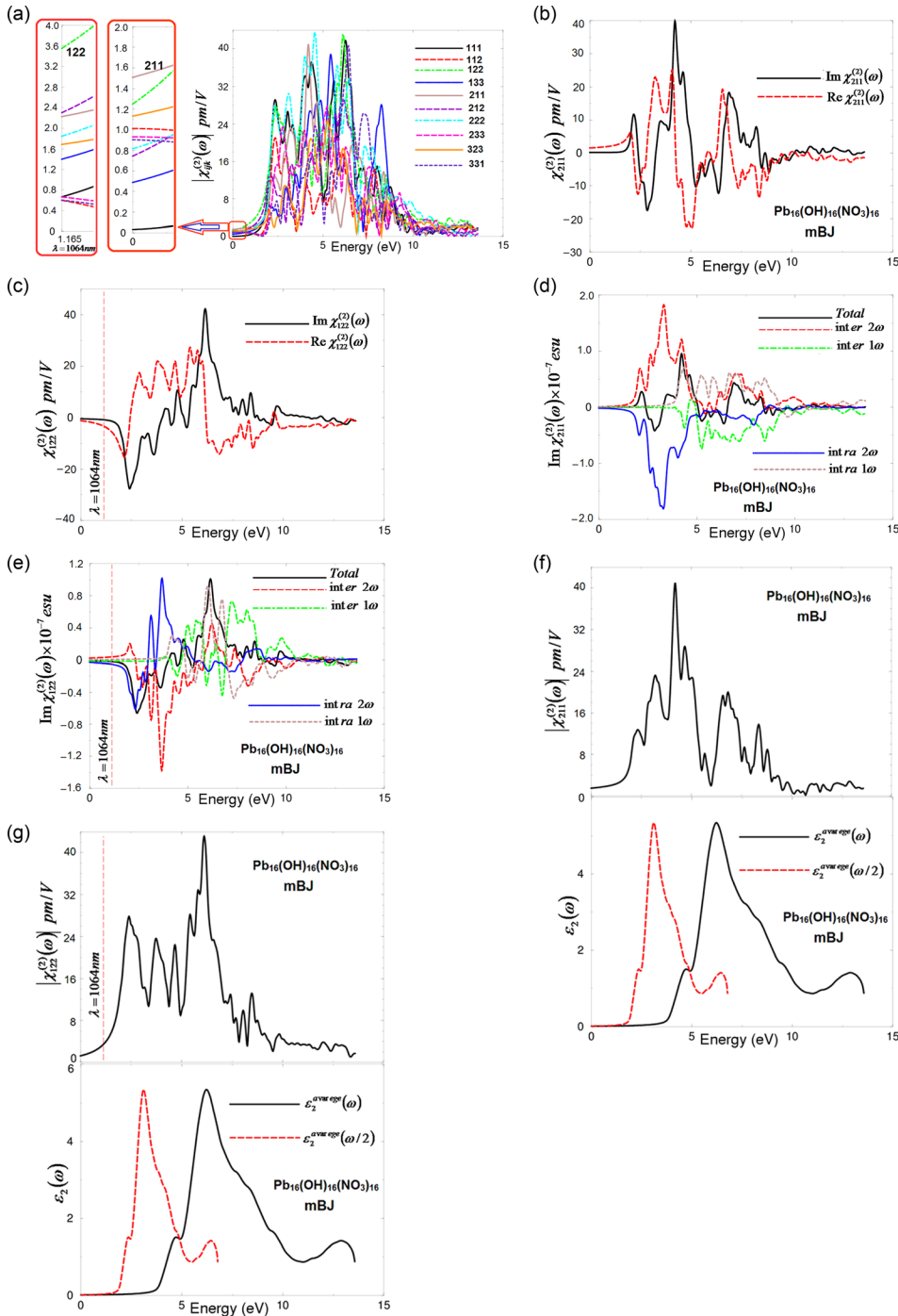
FIG. 2. (a) Calculated $|\chi_{ijk}^{(2)}(\omega)|$ for the ten tensor components of led nitrate hydroxide NLO crystal $Pb_{16}(OH)_{16}(NO_3)_{16}$; (b) calculated Imaginary $\chi_{211}^{(2)}(\omega)$ (dark solid curve-black) and real $\chi_{211}^{(2)}(\omega)$ (light dashed curve-red) spectra; (c) calculated Imaginary $\chi_{122}^{(2)}(\omega)$ (dark solid curve-black) and real $\chi_{122}^{(2)}(\omega)$ (light dashed curve-red) spectra; (d) calculated total Im $\chi_{211}^{(2)}(\omega)$ spectrum (dark solid curve-black) along with the intra $(2\omega)/(1\omega)$ (light solid curve-blue)/(light dashed doted curve-cyan) and inter $(2\omega)/(1\omega)$ (light long dashed curve-red)/(light doted curve-green)—band contributions, here all Im $\chi_{211}^{(2)}(\omega)$ are multiplied by 10^{-7}, in esu units; (e) calculated total Im $\chi_{122}^{(2)}(\omega)$ spectrum (dark solid curve-black) along with the intra $(2\omega)/(1\omega)$ (light solid curve-blue)/(light dashed doted curve-cyan) and inter $(2\omega)/(1\omega)$ (light long dashed curve-red)/(light doted curve-green)—band contributions, here all Im $\chi_{122}^{(2)}(\omega)$ are multiplied by 10^{-7}, in esu units; (f) -upper panel- calculated $|\chi_{211}^{(2)}(\omega)|$ (dark solid curve-black); -lower panel- calculated $\varepsilon_2^{xx}(\omega)$ (dark solid curve-black); calculated $\varepsilon_2^{xx}(\omega/2)$ (dark dashed curve-red); (f) -upper panel- calculated $|\chi_{122}^{(2)}(\omega)|$ (dark solid curve-black); -lower panel- calculated $\varepsilon_2^{xx}(\omega)$ (dark solid curve-black); calculated $\varepsilon_2^{xx}(\omega/2)$ (dark dashed curve-red).

in fulfilling the phase-matching conditions. The birefringence can be estimated from the refractive indices following the expression $\Delta n(\omega) = n_z(\omega) - n_x(\omega)$. Therefore, we have calculated the refractive indices from the complex dielectric function, as shown in Fig. 1(f). The calculated values of $n^{xx}(0) = n^{yy}(0)$, $n^{zz}(0)$, and $\Delta n(\omega)$ are shown in Table I, and the dispersion of the birefringence is illustrated in Fig. 1(g). It is clear that $Pb_{16}(OH)_{16}(NO_3)_{16}$ exhibits relatively large birefringence. Based on the discussion of Bian et al.[12] regarding the electron cloud of the BO_3 anionic groups which exhibit planar shape with conjugated electron orbitals, which make the BO_3 anionic groups the main source of the large birefringence in Pb_2BO_3F, therefore, similar to BO_3, the NO_3 can be the source of the large birefringence in $Pb_{16}(OH)_{16}(NO_3)_{16}$. The

electron cloud of the NO_3 anionic groups exhibits a planar shape with conjugated electron orbitals (see Fig. 1(h) and Fig. S1 of the supplementary material[19]). It is well-known that the birefringence determines partly whether an NLO material has the value of study.[12] Furthermore, Fig. 1(h) shows a high electron density configuration and strong anisotropy for N-O groups, which indicates the main contribution of NO_3 groups to the optical anisotropy.

B. Complex second-order non-linear optical dispersion

The $Pb_{16}(OH)_{16}(NO_3)_{16}$ nonlinear optical single crystal belongs to point group Cc. This symmetry allows only ten non-zero components of the second harmonic generation

TABLE II. Calculated $|\chi_{ijk}^{(2)}(\omega)|$ and β_{ijk} of $Pb_{16}(OH)_{16}(NO_3)_{16}$, in pm/V at static limit and at $\lambda = 1064$ nm, where 1 pm/V = 2.387×10^{-9} esu. The bold are the values of the dominate components.

		$Pb_{16}(OH)_{16}(NO_3)_{16}$		
Tensor components	$\chi_{ijk}^{(2)}(0)$	Theory $d_{ijk} = 0.5 \, \chi_{ijk}^{(2)}(\omega)$ at static limit	$\chi_{ijk}^{(2)}(\omega)$ at $\lambda = 1064$ nm	Theory $d_{ijk} = 0.5 \, \chi_{ijk}^{(2)}(\omega) \, \lambda = 1064$ nm
$\|\chi_{111}^{(2)}(\omega)\|$	0.042	$d_{11} = 0.021$	0.679	$d_{11} = 0.339$
$\|\chi_{112}^{(2)}(\omega)\|$	1.021	$d_{16} = 0.510$	0.560	$d_{16} = 0.280$
$\|\chi_{122}^{(2)}(\omega)\|$	1.272	$d_{12} = 0.636$	**3.558**	$d_{12} = 1.779$
$\|\chi_{133}^{(2)}(\omega)\|$	0.489	$d_{13} = 0.244$	1.416	$d_{13} = 0.708$
$\|\chi_{211}^{(2)}(\omega)\|$	**1.520**	$d_{21} = 0.760$	2.246	$d_{21} = 1.123$
$\|\chi_{212}^{(2)}(\omega)\|$	0.743	$d_{26} = 0.371$	2.339	$d_{26} = 1.169$
$\|\chi_{222}^{(2)}(\omega)\|$	0.823	$d_{22} = 0.411$	1.873	$d_{22} = 0.937$
$\|\chi_{233}^{(2)}(\omega)\|$	0.950	$d_{23} = 0.475$	0.636	$d_{23} = 0.318$
$\|\chi_{323}^{(2)}(\omega)\|$	1.134	$d_{34} = 0.567$	1.704	$d_{34} = 0.852$
$\|\chi_{331}^{(2)}(\omega)\|$	0.903	$d_{35} = 0.452$	0.602	$d_{35} = 0.301$
β_{122}	7.94×10^{-30} esu		22.89×10^{-30} esu	
β_{211}	9.47×10^{-30} esu		14.21×10^{-30} esu	

third rank tensor: $\chi_{111}^{(2)}(\omega)$, $\chi_{112}^{(2)}(\omega)$, $\chi_{122}^{(2)}(\omega)$, $\chi_{133}^{(2)}(\omega)$, $\chi_{211}^{(2)}(\omega)$, $\chi_{212}^{(2)}(\omega)$, $\chi_{222}^{(2)}(\omega)$, $\chi_{233}^{(2)}(\omega)$, $\chi_{323}^{(2)}(\omega)$, and $\chi_{331}^{(2)}(\omega)$. The formalism which is used to calculate the complex non-linear optical properties is presented elsewhere.[33–37] The nonlinear optical properties are calculated using the NLO code, which is compatible with the WIEN2k package, see Ref. 33. Therefore, based on the electronic band structure calculations, we have obtained the ten tensors as shown in Fig. 2(a). We would like to mention that, since the recently modified Becke-Johnson potential (mBJ) succeeds in bringing the calculated energy gap (3.7 eV) closer to the experimental one (3.78 eV),[15] therefore, we present the results of the mBJ only. It is well-known that the complex second-order non-linear optical properties are very sensitive to the energy band gap value; thus a quasi-particle self-energy correction at the level of scissors operators is further applied, which causes a rigid shift to the energy bands to bring the calculated energy gap to the exact experimental value.[35]

The SHG values of all tensor components at the static limit and at $\lambda = 1064$ nm are presented in Table II. It has been found that, from Table II and Fig. 2(a), the tensor component $\chi_{211}^{(2)}(\omega)$ is the dominant one at the static limit, while $\chi_{122}^{(2)}(\omega)$ is the dominant at $\lambda = 1064$ nm. Following Table II, we found that the obtained the SHG value of d_{21} at $\lambda = 1064$ nm shows a good agreement with the reported measured value.[15] It is found that the cost of good SHG performance is the narrow band gap, which limits the transmittance in the UV region. The main point to obtain NLO materials used in the UV region is getting the delicate balance between the SHG response and band gap.[13]

For more details about the dominant tensor components $\chi_{211}^{(2)}(\omega)$ and $\chi_{122}^{(2)}(\omega)$, the imaginary and real parts are presented in Figs. 2(b) and 2(c). From the imaginary part, it has been noticed that the 2ω terms oscillate at the half energy gap (1.89 eV) and the ω terms start to oscillate at the value of the fundamental energy gap (3.78 eV) to associate 2ω terms, while the tail of the imaginary part is originated from ω terms only. The real part is obtained from the existing information of the imaginary part by means of the Kramers-Kronig transformation.[33–37]

The imaginary and real parts are further separated into $2\omega/\omega$ inter-/intra-band contributions. Figs. 2(d) and 2(e) illustrate the $2\omega/\omega$ inter-/intra-band contributions of the imaginary part of $\chi_{211}^{(2)}(\omega)$ and $\chi_{122}^{(2)}(\omega)$, the dominant components at the static limit and at $\lambda = 1064$ nm. It is clear that the $2\omega/\omega$ inter-/intra-band contributions oscillate around zero and exhibit a considerable anisotropy. The sum of those contributions gives the total value of the imaginary part of the SHG.

To understand the origin of the SHG tensor components, we have analyzed the spectral features of $|\chi_{211}^{(2)}(\omega)|$ and $|\chi_{122}^{(2)}(\omega)|$. A step forward, the absorptive part of the corresponding dielectric function $\varepsilon_2(\omega)$ as a function of both $\omega/2$ and ω is associated with spectral structures of $|\chi_{211}^{(2)}(\omega)|$ and $|\chi_{122}^{(2)}(\omega)|$, as shown in Figs. 2(f) and 2(g). The spectral structures of $\varepsilon_2(\omega)$, $\varepsilon_2(\omega/2)$, $|\chi_{211}^{(2)}(\omega)|$, and $|\chi_{122}^{(2)}(\omega)|$ can be divided into three spectral regions. The spectral region confined between 1.89 eV ($E_g/2$) and 3.78 eV (E_g) is mainly formed by the 2ω resonance. The second structure between 3.78 eV (E_g) and 7.5 eV is associated with interference between 2ω and ω resonances, which is associated with the first spectral structure of $\varepsilon_2(\omega)$. It is clear that in this region the ω terms start to oscillate and contribute to the spectral structure of $|\chi_{211}^{(2)}(\omega)|$ and $|\chi_{122}^{(2)}(\omega)|$ in addition to 2ω terms. The third spectral structure from 7.5 eV to 13.5 eV is mainly due to ω resonance which is associated with the second structure in $\varepsilon_2(\omega)$.

C. Microscopic first hyperpolarizability

With the aid of the existing values for $\chi_{111}^{(2)}(\omega)$, $\chi_{112}^{(2)}(\omega)$, $\chi_{122}^{(2)}(\omega)$, $\chi_{133}^{(2)}(\omega)$, $\chi_{211}^{(2)}(\omega)$, $\chi_{212}^{(2)}(\omega)$, $\chi_{222}^{(2)}(\omega)$, $\chi_{233}^{(2)}(\omega)$, $\chi_{323}^{(2)}(\omega)$, and $\chi_{331}^{(2)}(\omega)$ of the $Pb_{16}(OH)_{16}(NO_3)_{16}$ nonlinear optical single crystal, we have obtained the values of the microscopic first hyperpolarizability, β_{ijk},[38] the vector component along the dipole moment direction, at the static limit and at $\lambda = 1064$ nm. We should emphasize that the β_{ijk} term cumulatively yield a bulk observable second order susceptibility term, $\chi_{ijk}^{(2)}(\omega)$, which in turn is responsible for the strong SHG response.[39] Since $\chi_{211}^{(2)}(\omega)$ is the dominate component at the static limit and $\chi_{122}^{(2)}(\omega)$ is the dominate component at $\lambda = 1064$ nm, we have presented in Table II the

values of β_{211} and β_{122} at the static limit and at the wavelength 1064 nm.

IV. CONCLUSIONS

The all-electron full-potential calculations within the generalized gradient approximation (PBE-GGA) and the recently modified Becke-Johnson (mBJ) potentials were used to perform comprehensive theoretical calculations for acentric $Pb_{16}(OH)_{16}(NO_3)_{16}$ single crystals. Using PBE-GGA, the experimental crystallographic data were optimized. The mBJ potential brings the calculated energy band gap very close to the measured one. The complex first-order linear optical dispersion reveals the existence of the considerable anisotropy between the optical components along x, y, and z polarization directions. The investigated crystal possesses a negative uniaxial anisotropy and positive birefringence. The calculated second harmonic generation shows that the tensor component $\chi_{211}^{(2)}(\omega)$ is the dominant one at the static limit, while $\chi_{122}^{(2)}(\omega)$ is the dominant at $\lambda = 1064$ nm. It has been found that the obtained SHG value of d_{21} at $\lambda = 1064$ nm exhibits a good agreement with the reported measured value. Using $\chi_{211}^{(2)}(\omega)$ and $\chi_{122}^{(2)}(\omega)$, we have obtained the values of β_{211} and β_{122} at the static limit and at $\lambda = 1064$ nm.

ACKNOWLEDGMENTS

[1]C. T. Chen, Y. C. Wu, A. D. Jiang, B. C. Wu, G. M. You, R. Li, and S. Lin, "New nonlinear-optical crystal LiB₃O₅," J. Opt. Soc. Am. B **6**, 616–621 (1989).

[2]P. S. Halasyamani and K. R. Poeppelmeier, "Noncentrosymmetric oxides," Chem. Mater. **10**, 2753–2769 (1998).

[3]P. A. Maggard, C. L. Stern, and K. R. Poeppelmeier, "Understanding the role of helical chains in the formation of noncentrosymmetric solids," J. Am. Chem. Soc. **123**, 7742–7743 (2001).

[4]C. F. Sun, C. L. Hu, X. Xu, B. P. Yang, and J. G. Mao, "Explorations of new second-order nonlinear optical materials in the potassium vanadyl iodate system," J. Am. Chem. Soc. **133**, 5561–5572 (2011).

[5]W. L. Zhang, W. D. Chen, H. Zhang, L. Geng, C. S. Lin, and Z. Z. He, "A strong second-harmonic generation material $Cd_4BiO(BO_3)_3$ originating from 3-chromophore asymmetric structures," J. Am. Chem. Soc. **132**, 1508–1509 (2010).

[6]S. L. Pan, J. P. Smit, B. Watkins, M. R. Marvel, C. L. Stern, and K. R. Poeppelmeier, "Synthesis, crystal structure, and nonlinear optical properties of $Li_6CuB_4O_{10}$: A congruently melting compound with isolated $[CuB_4O_{10}]$ 6- units," J. Am. Chem. Soc. **128**, 11631–11634 (2006).

[7]S. J. Choyke, S. M. Blau, A. A. Larner, S. A. Narducci, J. Yeon, P. S. Halasyamani, and A. Norquist, "Noncentrosymmetry in new templated gallium fluorophosphates," J. Inorg. Chem. **48**, 11277–11282 (2009).

[8]D. Xue and Z. Zhang, "Structural analysis of nonlinearities of $Ca_4ReO(BO_3)_3$ (Re = La, Nd, Sm, Gd, Er, Y)," Appl. Phys. A **68**, 57–61 (1999).

[9]R. C. Ramachandra, R. Gobinathan, and F. D. Gnanam, "Growth and characterisation of potassium pentaborate single crystals," Cryst. Res. Technol. **28**, 453–456 (1993).

[10]C. Chen, Y. Wang, Y. Xia, B. Wu, D. Tang, K. Wu, W. Zeng, L. Yu, and L. Mei, "New development of nonlinear optical crystals for the ultraviolet region with molecular engineering approach," J. Appl. Phys. **77**, 2268–2272 (1995).

[11]Y. Mori, I. Kuroda, S. Nakajima, T. Sasaki, and S. Nakai, "New nonlinear optical crystal: Cesium lithium borate," Appl. Phys. Lett. **67**, 1818 (1995).

[12]Q. Bian, Z. Yang, L. Dong, S. Pan, H. Zhang, H. Wu, H. Yu, W. Zhao, and Q. Jing, "First principle assisted prediction of the birefringence values of functional inorganic borate materials," J. Phys. Chem. C **118**(44), 25651–25657 (2014).

[13]D. Li, Q. Jing, C. Lei, S. Pan, B. Zhang, and Z. Yang, "Theoretical perspective of the lone pair activity influence on band gap and SHG response of lead borates," RSC Adv. **5**, 79882–79887 (2015).

[14]W. T. Dong, H. J. Zhang, Q. Su, Y. H. Lin, S. M. Wang, and C. S. Zhu, "Crystal growth, structure, and properties of new nonlinear optical materials: $K_2Ln(NO_3)_5 \cdot 2H_2O$ (Ln = La, Ce, Pr, Nd, Sm)," J. Solid State Chem. **148**, 302–307 (1999).

[15]L. Chang, L. Wang, X. Su, S. Pan, R. Hailili, H. Yu, and Z. Yang, "A nitrate nonlinear optical crystal $Pb_{16}(OH)_{16}(NO3)_{16}$ with a large second-harmonic generation response," Inorg. Chem. **53**, 3320–3325 (2014).

[16]P. Blaha, K. Schwarz, G. K. H. Madsen, D. Kvasnicka, and J. Luitz, *WIEN2k, An Augmented Plane Wave Plus Local Orbitals Program for Calculating Crystal Properties*, Vienna University of Technology, Austria (2001).

[17]J. P. Perdew, K. Burke, and M. Ernzerhof, "Generalized gradient approximation made simple," Phys. Rev. Lett. **77**, 3865–3868 (1996).

[18]F. Tran and P. Blaha, "Accurate band gaps of semiconductors and insulators with a semilocal exchange-correlation potential," Phys. Rev. Lett. **102**, 226401 (2009).

[19]See supplementary material at http://dx.doi.org/10.1063/1.4943650 for Fig. S1: Crystal structure of led nitrate hydroxide NLO crystal $Pb_{16}(OH)_{16}(NO_3)_{16}$ shows the local dipole moment of PbO_n polyhedra and $[NO_3]^-$ triangle. The local dipole moment of PbO_n polyhedra is larger than that of NO_3^- triangles. It can be seen that each two neighbors PbO_n polyhedra are oriented to the same directions while the $[NO_3]^-$ are almost randomly oriented. The net local dipole moment of the PbO_n polyhedra is oriented along a-c crystallographic plane. Fig. S2: The calculated electronic band structure using mBJ along with the measured optical absorption spectra of $Pb_{16}(OH)_{16}(NO_3)_{16}$ (Ref. 15) (left panel), which show the good agreement between the theory and the experiment in the mater of the value of the energy band gap. We have used a software to extract the experimental data from the figure provided in Ref. 15, then we re-plot the extracted data and compared with the electronic band structure. The right panel shows the calculated absorption coefficient of $Pb_{16}(OH)_{16}(NO_3)_{16}$ using mBJ which show the absorption edge of about 3.7 eV in comparison with the measured absorbance.[15] Fig. S3: (Left panel) The optical transitions depicted on a generic band structure of $Pb_{16}(OH)_{16}(NO_3)_{16}$ using mBJ. For simplicity, we have labeled the optical transitions as A, B, and C. The transitions (A) are responsible for the structures along $\varepsilon_2^{xx}(\omega)$, $\varepsilon_2^{yy}(\omega)$, and $\varepsilon_2^{zz}(\omega)$ in the spectral range 0.0–5.0 eV; the transitions (B) 5.0–10.0 eV, and the transitions (C) 10.0–14.0 eV; (intermediate panel) the calculated Pb-6s/6p, N-2p, O-2p, and H-1s partial density of states using mBJ; (right panel) the calculated Pb-5d/4f, N-2s, and O-2s partial density of states using mBJ. The intermediate and right panels show the orbitals which are responsible on the allowed optical transitions. Fig. S4: (left panel) The calculated band structure of $Pb_{16}(OH)_{16}(NO_3)_{16}$ using PBE-GGA; (intermediate panel) the calculated Pb-6s/6p, N-2p, O-2p, and H-1s partial density of states using PBE-GGA; (right panel) the calculated Pb-5d/4f, N-2s, and O-2s partial density of states using PBE-GGA. Fig. S5: (left panel) The calculated band structure of $Pb_{16}(OH)_{16}(NO_3)_{16}$ using mBJ which show that the energy band gap of about 3.70 eV; (right panel) The calculated band structure of $Pb_{16}(OH)_{16}(NO_3)_{16}$ using PBE-GGA which show that the energy band gap of about 3.13 eV. Calculations exhibit that the conduction band minimum (CBM) is situated at the center (Γ) of the Brillouin zone (BZ) while the valence band maximum (VBM) is located between Γ and Y points of the BZ, resulting in an indirect energy band gap. Table S1: The optimized lattice parameters using PBE-GGA in comparison with the experimental data.[15] Table S2: The optimized atomic positions using PBE-GGA in comparison with the experimental data.[15]

[20]K. Schwarz and P. Blaha, "Solid state calculations using WIEN2k," Comput. Mater. Sci. **28**, 259–273 (2003).

[21]M. Malachowski, I. R. Kityk, and B. Sahraoui, "Electronic structure and optical response in $Ga_xAl_{1-x}N$ solid alloys," Phys. Lett. A **242**, 337–342 (1998).

[22]I. Fuks-Janczarek, R. Miedzinski, M. G. Brik, A. Majchrowski, L. R. Jaroszewicz, and I. V. Kityk, "Z-scan analysis and Ab-initio studies of beta-$BaTeMo_2O_9$ single crystal," Solid State Sci. **27**, 30–35 (2014).

[23]C.-G. Ma and M. G. Brik, "First principles studies of the structural, electronic and optical properties of $LiInSe_2$ and $LiInTe_2$ chalcopyrite crystals," Solid State Commun. **203**, 69–74 (2015).

[24]F. Bassani and G. P. Parravicini, *Electronic States and Optical Transitions in Solids* (Pergamon Press Ltd., Oxford, 1975), pp. 149–154.

[25]C. Ambrosch-Draxl and J. O. Sofo, "Linear optical properties of solids within the full-potential linearized augmented planewave method," Comput. Phys. Commun. **175**, 1–14 (2006).

[26]See http://www.wien2k.at/reg_user/textbooks/usersguide.pdf for WIEN2k package.

[27]A. H. Reshak, "Specific features of electronic structures and optical susceptibilities of molybdenum oxide," RSC Adv. **5**, 22044–22052 (2015).

[28]A. H. Reshak, H. Huang, H. Kamarudin, and S. Auluck, "Alkali-metal/alkaline-earth-metal fluorine beryllium borate $NaSr_3Be_3B_3O_9F_4$ with large nonlinear optical properties in the deep-ultraviolet region," J. Appl. Phys. **117**, 085703 (2015).

[29]A. H. Reshak, "Transport properties of g-BC3 and t-BC3 phases," RSC Adv. **5**, 33632–33638 (2015).

[30]J. W. Lekse, M. A. Moreau, K. L. McNerny, J. Yeon, P. S. Halasyamani, and J. A. Aitken, "Second-harmonic generation and crystal structure of the diamond-like semiconductors Li_2CdGeS_4 and Li_2CdSnS_4," Inorg. Chem. **48**, 7516–7518 (2009).

[31]J. A. Brant, D. J. Clark, Y. S. Kim, J. I. Jang, Jian-H. Zhang, and J. A. Aitken, "Li_2CdGeS_4: A diamond-like semiconductor with strong second-order optical nonlinearity in the infrared and exceptional laser damage threshold," Chem. Mater. **26**, 3045–3048 (2014).

[32]D. R. Penn, "Wave-number-dependent dielectric function of semiconductors," Phys. Rev. B **128**, 2093 (1962).

[33]S. Sharma and C. Ambrosch-Draxl, "Second-harmonic optical response from first principles," Phys. Scr. T. **109**, 128 (2004).

[34]S. Sharma, J. K. Dewhurst, and C. Ambrosch-Draxl, "Linear and second-order optical response of III-V monolayer superlattices," Phys. Rev. B **67**, 165332 (2003).

[35]S. N. Rashkeev, W. R. L. Lambrecht, and B. Segall, "Efficient Ab initio method for the calculation of frequency-dependent second-order optical response in semiconductors," Phys. Rev. B **57**, 3905 (1998).

[36]J. L. P. Hughes and J. E. Sipe, "Calculation of second-order optical response in semiconductors," Phys. Rev. B **53**, 10751 (1996).

[37]D. E. Aspnes, "Energy-band theory of the second-order nonlinear optical susceptibility of crystals of zinc-blende symmetry," Phys. Rev. B **6**, 4648 (1972).

[38]R. Y. Boyd, *Principles of Nonlinear Optics* (Academic Press, NY, 1982), p. 420.

[39]R. W. Boyd, *Nonlinear Optics*, 3rd ed. (Academic Press is an imprint of Elsevier, 2008).